Information Sciences 500 (2019) 67–86

Contents lists available at ScienceDirect

Information Sciences

journal homepage: www.elsevier.com/locate/ins

Enhancement of dronogram aid to visual interpretation of target objects via intuitionistic fuzzy hesitant sets

Biswajit Biswas[a,b], Siddhartha Bhattacharyya[b,c,*], Jan Platos[a,b], Vaclav Snasel[a,b]

[a] Department of Computer Science and Engineering, University of Calcutta, Kolkata, West Bengal, India
[b] Faculty of Electrical Engineering and Computer Science, VSB Technical University of Ostrava, Ostrava, Czech Republic
[c] RCC Institute of Information Technology, Kolkata, India

ARTICLE INFO

Article history:
Received 20 October 2018
Revised 19 May 2019
Accepted 26 May 2019
Available online 28 May 2019

Keywords:
Visual enhancement
Drone image
Fuzzy set
Intuitionistic fuzzy set
Hesitant set
Hesitant score.

ABSTRACT

In this paper, we address the hesitant information in enhancement task often caused by differences in image contrast. Enhancement approaches generally use certain filters which generate artifacts or are unable to recover all the objects details in images. Typically, the contrast of an image quantifies a unique ratio between the amounts of black and white through a single pixel. However, contrast is better represented by a group of pixels. We have proposed a novel image enhancement scheme based on intuitionistic hesitant fuzzy sets (IHFSs) for drone images (dronogram) to facilitate better interpretations of target objects. First, a given dronogram is divided into foreground and background areas based on an estimated threshold from which the proposed model measures the amount of black/white intensity levels. Next, we fuzzify both of them and determine the hesitant score indicated by the distance between the two areas for each point in the fuzzy plane. Finally, a hyperbolic operator is adopted for each membership grade to improve the photographic quality leading to enhanced results via defuzzification. The proposed method is tested on a large drone image database. Results demonstrate better contrast enhancement, improved visual quality, and better recognition compared to the state-of-the-art methods.

1. Introduction

I n computer vision, contrast enhancement is the only method that is used to improve the visibility of underexposed image details. Due to the limitation in the imaging sensors (viz. camera), low illumination, poor quality imaging acquisition systems and improper settings (viz. lenses), the contrast of the captured images can be distinct from ground-truth. For a better human perception and understanding, improvement in the quality of the acquired images is a mandatory requirement. To obtain an enhanced image with better details from these low dynamic range images, contrast enhancement is performed on the basis of image processing criteria [2,11,29,30]. Presently, the application of unmanned aerial vehicles (UAVs viz. Drone) is rapidly growing in various fields such as surveillance, military, agriculture, etc. in incommodious environments. Object detection and tracking are very challenging tasks in the field of intelligent transportation and automatic

* Corresponding author at: RCC Institute of Information Technology, Kolkata, India.
E-mail addresses: biswajit.cu.08@gmail.com (B. Biswas), siddhartha.bhattacharyya@vsb.cz (S. Bhattacharyya), jan.platos@vsb.cz (J. Platos), vaclav.snasel@vsb.cz (V. Snasel).

https://doi.org/10.1016/j.ins.2019.05.069

monitoring [15,16,18]. Typically, the targets often include vehicles, vessels, crafts, traffic signs, cars or forest; such targets are specifically highly informative, which can be used to improve the accuracy of target tracking (e.g., vessel shape and grouping activity are used in order to differentiate and predict the vessel), and prior spatial information aid to recognize the detection of target objects (viz. vessels, trees, house) [16,18]. Due to the expensive nature of drone devices, the processing cost is very high for fast dynamic motion and transmission. Moreover, the projected drone images can be deteriorated by various noises, degraded normal illumination and visual quality [15,16,27]. Consequently, it is essential to design and implement a drone efficient image enhancement algorithm with higher accuracy to understand and recognize target objects so as to address the better discrimination of specific objects in dronogram without increasing the burden of the hardware costs [15,27].

In past few decades, researchers have tried to solve the exact contrast enhancement problem for colour imaging using several approaches [2,6,24,29,30,38]. Improved contrast and image details are often required in a wide range of computer vision applications but a generic solution to this problem has not been discovered. Several enhancement methods have been suggested such as spatial filtering, histogram equalization (HE), wavelet decomposition, or soft computing (fuzzy sets, neuro-fuzzy, convolutional neural networks) theory [4,9,19,30]. All these methods are broadly classified into spatial-domain and transformation-domain methods. Detailed reviews can be found in [5,12,29,30,33].

Spatial-domain methods: These methods are built on the straightforward manipulation of pixel intensities in source images [2,4,11,30,37]. Mainly, statistical based sub-band filtering approaches have been utilized to enhance underexposed and low illumination in target images by suppressing noise [2,23,30], but these techniques perhaps cause edge blurring and detail loss [2,4,19,30]. Thus, adaptive enhancement approaches are beneficial to improve the contrast while maintaining edges and details of dronograms [2,5,12,30]. The adaptive density weighted contrast [2,11,30], or first derivative and local statistics [2,12,30] are common adaptive based approaches. Though histogram equalization (HE) techniques retain the predominant view in the field of enhancement, they possibly result in unnecessary contrast enhancement or over-fit brightness effect resulting from the lack of constraint on the level of enhancement [2,6,25,30,38]. Thus, some techniques are investigated to overcome those lacks, e.g., the adaptive HE (AHE), and contrast limited AHE (CLAHE) [2,5,29,30,33] in literature. Unsharp masking (UM) is useful for enhancing exact details of dronograms, but increases noise and exceeds steep details at the same moment [2,25,29,30]. Later, few revised methods such as the rational UM [2,30] and nonlinear UM (NUM) [2,12,25,30] have been suggested to overcome those problems.

Recently, deep learning is achieving impressive state-of-the art performance for different image processing tasks such as image segmentation, image enhancement etc. [7,32,43]. Deep convolutional neural network architecture is quickly becoming prominent in image processing since it provides the ability to efficiently encode spectral and spatial information based on the input image data, without any prepossessing step. It consists of multiple interconnected layers and learns a hierarchical feature representation from raw pixel-data. It discovers features at multiple levels of representations. Several researchers have suggested various deep learning based image enhancement methods such as Deep Bilateral Learning [10], deep convolutional neural network based image enhancement [34,39], Dehaznet for image enhancement [3], MSR-net [31,34] etc. All the deep learning based image enhancement methods produce remarkable results for real time images and low illuminated images. Therefore, deep learning method is most robust but lots of synthetic data as well as high computational resources are required to perform the deep learning algorithms. Sometimes, deep learning approaches suffer from high bias and over-fitting problem due to the nature of data.

Transformation-domain methods: In this case, all existing techniques are designed based on the multi-scale representation or Fourier transform approach, which often uses an input/output transformation that varies with the regional feature of a dronogram. Firstly, multi-scale representation-based schemes decompose an image into a level of multi-scale sub-bands by using the contourlet, discrete dyadic wavelet, complex wavelets or shearlet [2,17,25,30]. However, most wavelet based schemes are unable to preserve both the contour and geometry of edges in images [17,29,30] whereas contourlet and shearlet are better for preserving image details. Moreover, traditional transformation-domain techniques can produce artefacts such as undesirable blocking effects [19,23,29,30], or enhance image uniformly, but incompletely enhance all regional image details/regions [6,18,26,38]. Still, implementation and run-time costs for contourlet or shearlet are complicated issues in real-time applications [2,25,30].

Since uncertainty and vagueness are undoubtedly created during the acquisition or transmission of images, a reliable model interpreting such images should use the personal experience to determine heuristically. Although, this can be construed by the classical mathematical modeling [4,6,29,30,38]. Hence, fuzzy sets (FSs), logical FSs, type-I FSs, type-II FSs, or intuitionistic FSs (IFSs), have been used to improve the contrast and visual quality of images because they are knowledge-based systems. These fuzzy techniques efficiently process faulty data collected from imprecision and vagueness [2,29,30]. In most of the cases, the grey-level range of a contrast enhanced image using type-I FSs is relatively consistent, and inadequate to enhance the corrupted images with short grey levels and low-intensity values [4,19,30]. Type-II FSs are tough to practice and insufficient to address the exact hesitancy in ambiguity [6,23,26,30,38]. Consequently, image enhancement is basically a challenging task in the domain of image processing.

Lots of researchers have suggested various methods to enhance low-contrasted images and most of them perform quite efficiently [2,5,11,12,30,37]. Most of the existing methods cannot achieve the desired enhancement result for underexposed and low-illuminated images and typically suffer from deficiency with robustness and accuracy. Here, we propose an appropriate and fittest model to correct the intensity distribution of pixels in the image, which is suitable for human perception. To plan a dronogram (drone image) enhancement scheme, it is motivating to select intuitionistic fuzzy hesitant sets (IFHSs) theory because IFHS take into account more uncertainties in the form of membership function that is more bound to the as-

pects of human decision-making, in comparison to traditional FSs [1,19,41]. The IFHS is well-known for its power to measure hesitant quantity while addressing uncertainty in image information [4,6,28,38,40].

Inspired by literature study, a novel dronogram enhancement algorithm motivated by the IFHS theory has been developed in this paper. The proposed scheme is designed by using the hyperbolic regularization approach in the intuitionistic fuzzy hesitant set. We have formulated a different membership grades generator to construct the intuitionistic fuzzy hesitant set to measure the hesitant score in fuzzy membership grades under certain fuzzy enhancing criterion. The proposed framework has been divided into two main stages. First, we have separated the background-foreground areas utilizing the global threshold and constructed membership functions in the fuzzy domain. Secondly, a nonlinear real-valued hyperbolic function is applied to modify and adjust both the memberships in background-foreground areas to enhance source drone images. To increase the clarity of the dim image for object detection task, we have utilized adaptive threshold instead of direct or fixed threshold for the separation of foreground/ background of the image. Since low illuminated images are ambiguous in nature, we have applied hesitant score through intuitionistic fuzzy set for the enhancement task. The designed algorithm involves few parameters and thus the suggested scheme is automated and does not require any expert knowledge. Experimental results verify that the designed method is an efficient and simple way to improve the contrast and visual clarity in the dronogram. More detailed contributions are given below:

(1) We have proposed a novel enhancement scheme based on the hesitant fuzzy set theory for drone images. The proposed method effectively identifies foreground/background pixels in drone image for contrast correction with a global threshold in less execution time.
(2) We address hesitant information measure on foreground/background image areas and derive weighted parameters applying the hesitant score and hesitant distance function in foreground/background areas.
(3) To achieve the best membership grades, we have applied hyperbolic membership grade manipulation in the hesitant fuzzy set. Hyperbolic regularization has been exploited on the uncertainty of hesitancy using the hesitant score to determine and process image pixels low light images.
(4) We have revealed a unique enhancement process to adjust different pixel intensity ranges and brightness adaptation using fuzzy data integration.
(5) The result section shows that the proposed method outperforms the state-of-the-art algorithms while obtaining identical contrast enhancing results for target object detection.

The rest of this paper is structured as follows: In Section 2, we present the preliminaries to the related work. In Section 3, we illustrate the designed dronogram enhancement algorithm in details. In Section 4, we give experimental results and discussions. Conclusions and perspectives are presented in Section 5.

2. Preliminaries

This section concisely discusses the theories of intuitionistic fuzzy sets, hesitant fuzzy sets, and the basic framework of fuzzy image enhancement for drone imaging. The novel enhancement scheme is developed on the basis of the following concepts.

2.1. Fuzzy sets

According to mathematical definition in fuzzy theory [1,41], let $\mathbf{X} = \{x_1, x_2 \dots x_n\}$ is a reference of point set. The fuzzy set $\mathbf{A} = \{\langle x, \mu_A(x)\rangle | \forall x \in \mathbf{X}\}$ is defined on $\mathbf{X}$ by a membership function $\mu_A(x)$ for each generic points of $\mathbf{X}$. The membership function $\mu_A(x)$ is real-valued function such that μ_A: $x \to [0, 1]$, $x \in \mathbf{X}$ mapping each point of $\mathbf{X}$ into real line $\mathbb{R}$. $\mathbf{X}$ is a crisp set when $\mu_A(x)$ takes only 1 or 0 [1,40,41].

In fuzzy set, a digital image is defined by an array of singletons as membership grades of each pixel. Let $\mathbf{I}$ be a 2D image with size $\mathbf{P} \times \mathbf{Q} = \mathbf{N}$ containing $\mathbf{N}$ pixels with intensity levels in the dynamic range $(0, \mathbf{L} - \mathbf{1})$, thus a fuzzy set $\mathcal{I}$ is written as follows [1,6,19,29,41,42]:

$$\mathcal{I} = \bigcup_{i=1}^{\mathbf{P}} \bigcup_{j=1}^{\mathbf{Q}} \frac{\mu_{ij}(\mathbf{X})}{\mathbf{x_{ij}}}$$

where $\mu_{ij}(x)$ denotes the membership grades of intensity levels of each pixel $\mu_{ij}(x) \in \mathbf{I}$ in image $\mathbf{I}$ with size $\mathbf{P} \times \mathbf{Q} = \mathbf{N}$. **L, P, Q** and **N** are respectively the highest intensity levels (for 8-bit, $\mathbf{L} = 256$), width, height and total count of pixels in $\mathbf{I}$. Due to problem definition in image processing, the membership function $\mu_{ij}(x) \in \mathbf{I}$ for an image can be different. Several functions such as **triangulation, Gaussian, Bel-shape, S**-function are used as the membership function in literature [1,19,21,41].

2.2. Intuitionistic fuzzy sets and its construction

According to Atanassov [1], typically a fuzzy set considers only membership function $\mu(x) \in \mathbf{X}$ whereas an intuitionistic fuzzy set (IFS) deals with a membership function as ($\mu(x)$: $x \to [0, 1]$, $x \in \mathbf{X}$) with another special real-valued function known

as non-membership function such as ($\nu(x)$: $x \to [0, 1]$, $x \in \mathbf{X}$) on $\mathbf{X}$. Thus, an IFS for a point set $\mathcal{A}$ under discourse $\mathcal{X}$ is defined as follows [1,8,23]:

$$\mathcal{A} = \{\langle x, \mu_A(x), \nu_A(x)\rangle | x \in \mathcal{X}\} \tag{1}$$

where $\mu_A(x)$ and $\nu_A(x)$ are membership and non-membership grades of a point $\mathbf{x}$ belonging to the set $\mathcal{A} \subseteq \mathcal{X}$ under the following conditions [1,8,23]:

$$0 \le \mu_A(x) + \nu_A(x) \le 1$$

If $\nu_A(x) = 1 - \mu_A(x)$ for $\forall x \in \mathcal{A}$, then $\mathcal{A}$ becomes a fuzzy set (FS). For all intuitionistic fuzzy sets (IFSs), due to lack of knowledge to determine the membership grade of each point $\mathbf{x} \in \mathcal{A}$, a hesitation can been considered. Now, the hesitation is defined by a real-valued function ($\pi(x) : x \to [0, 1], x \in \mathcal{A}$) for $\mathcal{A} \subseteq \mathcal{X}$ as follows [1,8,40]:

$$\pi_A(x) = 1 - \mu_A(x) - \nu_A(x), \ \forall x \in \mathcal{A}$$

where, $\pi_A(x)$ represents the hesitation degree of $\mathbf{x} \in \mathcal{A}$ under interval

$$[\mu_A(x), \mu_A(x) + \nu_A(x)]$$

According to Atanassov [1,8], $f : x \to [0, 1], x \in \mathcal{X}$ is a continuous monotone function and monotone IFS constructor if $f(x)$ satisfies the following conditions [1,20,28]:

$$f(x) \le (1 - x)| \ \forall x \in \mathcal{A} \text{ and } f(0) = 1, f(1) = 0, \tag{2}$$

We have devised an IFS generator for the proposed model of the non-membership grade $\nu_A(x), x \in \mathcal{A}$ for IFS $\mathcal{A}$ through Yager's intuitionistic fuzzy complements [20,28] and Sugeno's [20,28] negation function. The IFS construction functions as IFS generator $\mathbf{N}(x)$ for IFS $\mathcal{A}$ in terms of intuitionistic fuzzy complements and negation functions which have been determined by modification of intuitionistic fuzzy complements, negation functions by the following expressions [8,20,28]:

$$N_1(x) = (1 - x^\alpha)^{\frac{1}{\alpha}}, \ \alpha > 0, \tag{3}$$

$$N_2(x) = \frac{1 - x^\alpha}{1 + \lambda x^\alpha}, \ \alpha > 0, \ \lambda > 0 \tag{4}$$

Both $N_1(x), N_2(x)$ satisfy $N_i(0) = 1, N_i(1) = 0, i = 1, 2$. Hence, we define our IFS generator $N(x)$ by using Eqs. (3) and (4) as follows:

$$N(x) = N_1(x) \cdot N_2(x) \tag{5}$$

$$N(x) = (1 - x^\alpha)^{\frac{1}{\alpha}} \cdot \left(\frac{1 - x^\alpha}{1 + \lambda x^\alpha}\right)$$
$$N(x) = \left[\frac{(1 - x^\alpha)^k}{1 + \lambda x^\alpha}\right], \ k = \left(1 + \frac{1}{\alpha}\right) \tag{6}$$

where, $N(x)$ always satisfies $N(0) = 1, N(1) = 0$ and $\alpha > 0, \lambda > 0$, respectively.

By using Eq. (6), IFS $\mathcal{A}$ in Eq. (1) is given by

$$\mathcal{A}_{(\alpha,\lambda)} = \left\{\left\langle x, \mu_A(x), \left[\frac{\left(1 - \mu_A(x)^\alpha\right)^k}{1 + \lambda \mu_A(x)^\alpha}\right]\right\rangle : x \in \mathcal{A}\right\} \tag{7}$$

and its hesitation degree π_A becomes

$$\pi_{\mathcal{A}}(x) = \left\{1 - \mu_A(x) - \left[\frac{\left(1 - \mu_A(x)^\alpha\right)^k}{1 + \lambda \mu_A(x)^\alpha}\right]\right\} \tag{8}$$

On the other hand, we can measure the non-membership function ν_A by using Yager's generator as follows [8,20,28]:

$$\nu_{\mathcal{A}}(x) = \left\{\left(1 - \mu_A(x)^\alpha\right)^k\right\} \tag{9}$$

Based on the aforesaid description, the IFS for an image $\mathbf{I}$, notionally, $\mathcal{A}^{\mathbf{I}}_{(\alpha,\lambda)}$ is defined by Eqs. (1) and (7) as follows:

$$\mathcal{A}^{\mathbf{I}}_{(\alpha,\lambda)} = \{\langle x_i, \mu_A(x_i), \nu_A(x_i), \pi_A(x_i)\rangle : i = 1, 2, \ldots, \mathbf{N}\} \tag{10}$$

where, $\mu_A(x_i)$, $\nu_A(x_i)$, and $\pi_A(x_i)$ are denoted as membership, non-membership and hesitant grades of the ith pixel of image $\mathbf{I}$. It is noted that, for different values of parameter α in fuzzy plane, the contrast of an image changes from high to dim or

vice versa. In the proposed method, the value of α is related to the image enhancement task, i.e. the contrast of an image can be controlled by adjusting the parameter α.

Before fuzzification, first, we have used the gray-level normalization procedure to normalize each source image. On the other hand, for defuzzification (viz. the inverse fuzzy map), we have utilized inverse gray-level normalization procedure [6,19,25]. In this paper, the fuzzy membership $\mu_A(x_i)$ for IFS $\mathcal{A}_{(\alpha,\lambda)}$ is defined in terms of normalized intensity levels of image **I** by following expression [6,19,41]:

$$\mu_A(x_i) = \left[\frac{\mathbf{x}_i - \mathbf{x}_{L_{\min}}}{\mathbf{x}_{L_{\max}} - \mathbf{x}_i}\right],\ i = 1, 2, \ldots, \mathbf{N} \tag{11}$$

where, **N** quantifies the total count of pixels, $\mathbf{x}_{L_{\max}}$ and $\mathbf{x}_{L_{\min}}$ specify the maximum and minimum gray level (**L**) of the image **I**, respectively. Eq. (11) is applied to transfer the pixel intensity of image to the fuzzy domain i.e., the membership grades $\mu_A^I(x)$ of the corresponding gray levels.

Intuitionistic fuzzy set theory mainly deals with two uncertainties-membership and non-membership degrees. As the choice of the membership function is dependent on the types of problems and differs from problem to problem, often a distinct function is used as hesitant when defining the membership function. Mostly, the membership function may be triangular, trapezoid, Gaussian, Gamma, Cauchy etc. In the intuitionistic fuzzy set, the non-membership degree is equal to the complement of the membership degree due to the existence of hesitant property.

2.3. Hesitant fuzzy sets and its construction

A hesitant fuzzy set (HFS) $\mathcal{A}$ in $\mathcal{X}$ is defined as [8,23,26]:

$$\mathcal{A} = \{\langle x, h_{\mathcal{A}}(x)\rangle : x \in \mathcal{X}\} \tag{12}$$

where, $h_{\mathcal{A}}(x) : x \to [0, 1], \forall x \in \mathcal{X}$ is a set of different values in [0, 1] denoting membership degrees of point **x** to $\mathcal{A}$ and is known as the hesitant fuzzy element (HFE) [23,26,40]. HFS $\mathcal{A}$ can be defined as a fuzzy set (FS) if there is only one element belonging to $h_{\mathcal{A}}(x)$ or a intuitionistic fuzzy set (IFS) if there are two elements present in $h_{\mathcal{A}}(x)$ [8,28,40].

According to Xia *et al.* [40], the hesitant normalized Hamming distance measure function is typically used to determine the distance between two HFSs. To measure on HFSs, given two HFSs $\mathcal{A}$ and $\mathcal{B}$, $h_{\mathcal{A}}^{\sigma(j)}(x_i)$ and $h_{\mathcal{B}}^{\sigma(j)}(x_i)$ represent j^{th} values in $h_{\mathcal{A}}(x_i)$ and $h_{\mathcal{B}}(x_i)$, which are defined on $\mathcal{X}$ such that $\forall x_i \in \mathcal{X}$; $(1 \le i \le n)$. The hesitant normalized Hamming distance (HNHD) is then given as [28,40]:

$$\mathbf{d}_h(\mathcal{A}, \mathcal{B}) = \frac{1}{n}\sum_{i=1}^{n}\left[\frac{1}{\mathbf{c}_{x_i}}\sum_{j=1}^{\mathbf{c}_{x_i}}\left|h_{\mathcal{A}}^{\sigma(j)}(x_i) - h_{\mathcal{B}}^{\sigma(j)}(x_i)\right|\right] \tag{13}$$

$$\mathbf{c}_{x_i} = \max_i\left\{\mathbf{c}\left(h_{\mathcal{A}}^{\sigma(j)}(x_i)\right), \mathbf{c}\left(h_{\mathcal{B}}^{\sigma(j)}(x_i)\right)\right\} \tag{14}$$

where, $\mathbf{c}\left(h_{\mathcal{A}}^{\sigma(j)}(x_i)\right)$, $\mathbf{c}\left(h_{\mathcal{B}}^{\sigma(j)}(x_i)\right)$ are the cardinal numbers and $h_{\mathcal{A}}^{\sigma(j)}(x_i)$, $h_{\mathcal{B}}^{\sigma(j)}(x_i)$ denote the ith highest value in $h_{\mathcal{A}}^{\sigma(j)}(x_i)$, $h_{\mathcal{B}}^{\sigma(j)}(x_i)$, respectively.

The Hesitant Score (HS) $[\mathcal{S}_{HS}(\cdot)]$ usually measures the amount of hesitance in a hesitant fuzzy set (HFS). The hesitant score for two HFSs such as $h_{\mathcal{A}}(x_i)$ and $h_{\mathcal{B}}(x_i)$ are given as [8,23,26,40]:

$$\mathcal{S}_{HS}^{\mathcal{A}}(\cdot) = \frac{1}{n}\sum_{i=1}^{n}\left[\frac{1}{\mathbf{c}_{x_i}}\sum_{j=1}^{\mathbf{c}_{x_i}}h_{\mathcal{A}}^{\sigma(j)}(x_i)\right] \tag{15}$$

$$\mathcal{S}_{HS}^{\mathcal{B}}(\cdot) = \frac{1}{n}\sum_{i=1}^{n}\left[\frac{1}{\mathbf{c}_{x_i}}\sum_{j=1}^{\mathbf{c}_{x_i}}h_{\mathcal{A}}^{\sigma(j)}(x_i)\right] \tag{16}$$

where, n denotes the number of elements in $h_{\mathcal{A}}(x_i)$ and $h_{\mathcal{B}}(x_i)$, respectively.

In order to construct the hesitant fuzzy set (HFS) in terms of intuitionistic fuzzy set (IFS), we adopt Eqs. (7)–(10). The membership degrees in a HFS may be different [23,26]. For exact measure, the cardinality $\mathbf{c}_x(\cdot)$ of both the two HFS $h_{\mathcal{A}}(x_i)$ and $h_{\mathcal{B}}(x_i)$ should be equal. If elements in $h_{\mathcal{A}}(x_i)$ are fewer than in $h_{\mathcal{B}}(x_i)$, then $h_{\mathcal{A}}(x_i)$ is enlarged by repeating its maximum element until its cardinality $\mathbf{c}_{\mathcal{A}}(\cdot)$ becomes equal to that of $\mathbf{c}_{\mathcal{B}}(\cdot)$ of $h_{\mathcal{B}}(x_i)$ [8,26,40].

If $\mathcal{A}, \mathcal{B} \subseteq \mathcal{X}$ and $\forall x \in \mathcal{X}$, then the two HFSs such as $h_{\mathcal{A}}(x_i)$, $h_{\mathcal{B}}(x_i)$ using Eq. (10) are considered as intuitionistic fuzzy hesitant sets (IFHSs) which are given as follows:

$$h_{\mathcal{A}}(x_i) = \{\langle x_i, \mu_A(x_i), \nu_A(x_i), \pi_A(x_i)\rangle : i = 1, 2, \cdots \mathbf{N}\} \tag{17}$$

$$h_{\mathcal{B}}(x_i) = \{\langle x_i, \mu_B(x_i), \nu_B(x_i), \pi_B(x_i)\rangle : i = 1, 2, \cdots \mathbf{N}\} \tag{18}$$

2.4. Outline of fuzzy image enhancement

In fuzzy image processing, there are three steps associated with the process of handling spatial image data, mostly [6,25,30,41]: (i) Fuzzification Λ, i.e., the input data $\mathbf{A} \subset \mathbf{X}$ (histograms, gray levels, features, etc.) is converted into a membership plane. (ii) Manipulation Φ, i.e., few algebraic as well as a logical operator (addition, multiplication, AND/OR) are used for proper modifications of the membership grades in a fuzzy plane for the enhancement and threshold. (iii) Defuzzification Ξ, i.e., if necessary, the modified membership in the fuzzy plane has to be inversely mapped into the characteristic plane (crisp set) without loss of generality. The output $\mathbf{X}$ of the fuzzy system for an input $x \in \mathbf{A}$ is given by the following processing stage as:

$$\mathbf{A} = \Xi(\Phi(\Lambda(\mathbf{X}))) \tag{19}$$

A fresh fuzzy membership function can be defined from the membership function of the input image. For an intuitionistic fuzzy set, Sugenoâs and Yagerâs intuitionistic fuzzy generators are used to find the non-membership function and the hesitant function. The hesitant score is utilized to find the optimum divergence value. In case of an intuitionistic fuzzy hesitant set, hyperbolized operators are used to reform a new membership function from the two membership levels of background/foreground areas. The proposed hyperbolized modifier is used to find the fittest shape of membership grades. The main distinction from other systems is that in image processing, the input data $\mathbf{X}$ is managed in the membership plane using the variety of FSs, IFSs, fuzzy logical, or fuzzy measure theories to modify and/or aggregate membership values, or to classify data, decision making, logical inferences, etc. [19,30,41]. The new membership values are re-transformed into the pixel plane to form new features in terms of histograms and gray levels [2,41].

3. Proposed methodology

Combining the hesitant information with nonlinear hyperbolic operators, we have introduced a novel fuzzy enhancement scheme in this study, which is based on intuitionistic fuzzy hesitant sets (IFHSs), called as DIEM for drone image enhancement. The proposed DIEM model is devised in terms of intuitionistic fuzzy set, hesitant measure and hyperbolic method which are described below.

3.1. DIEM scheme

In order to enhance an image, it is essential to separate the image into foreground and background portions because of correlation in both spatial and frequency domains. Foreground/background areas are used to quantify the amount of brightness to the blackness of an image. The division of an image into a foreground/background is illustrated in Fig. 3(a)–(c). Initially, a given original dronogram $\mathbf{I}(x)$ is divided into foreground region $\mathbf{I}_f(x)$ and background area $\mathbf{I}_b(x)$ via a threshold θ. Then, rearranged areas ($\mathbf{I}_f(x)$ and $\mathbf{I}_b(x)$) are processed through several fuzzy operations. The processed dronogram $\mathbf{D}(x)$ is assembled with the source image via different orders of fuzzy transforms to obtain a final enhanced dronogram $\mathbf{I}_e(x)$ using fuzzy regularization. The schematic diagram of the DIEM scheme is shown in Fig. 1. The different stages of dronogram enhancement by an intuitionistic fuzzy hesitant approach are scheduled as follows:

Step 1: Divide a dronogram ($\mathbf{I}(x)$) into the foreground ($\mathbf{I}_f(x)$) and background ($\mathbf{I}_b(x)$) image areas.
Step 2: Construct the hesitant intuitionistic fuzzy sets for the foreground and background regions by transforming the image plane into a fuzzy plane.
Step 3: Modify membership degrees by applying the hyperbolic operations on the foreground and background regions.
Step 4: Apply defuzzification entailing an inverse transform followed by merging the processed data with the source image data to obtain the enhanced image.

3.2. Separation of dronogram

The foreground/background separation is widely used in object detection task for contrast enhancement methods. This approach is adopted in order to measure whiteness/blackness of an image. Deng *et al.* have suggested an efficient utilization of the foreground/background separation in the dronogram enhancement task [6]. Typically, the foreground portion of an image includes the image details (viz. edge, corner, etc.) whereas the background represents smooth image information. Besides, the overall pixel intensity in the background area is shorter than the pixel intensity in the background area of an image. Because of different illuminations in foreground/background areas, the foreground/background areas play a key role in the image enhancement task.

To separate the foreground/background of an image, we calculate an optimal adaptive threshold instead of a direct or a fixed threshold. The threshold value plays a crucial role for the foreground/background seperation task to quantify the image pixels and assures the convergence of the algorithm. Our aim to choose an optimal thresholds which reduce the number of iterations as well as execution time. We have introduced an iterative approach to divide a dronogram ($\mathbf{I}$) into foreground ($\mathbf{I}_f$) and background ($\mathbf{I}_b$) portions automatically. For a given source dronogram ($\mathbf{I}$), the following strategy has been utilized to determine a global threshold (θ) based on the mean μ_I of ($\mathbf{I}$).

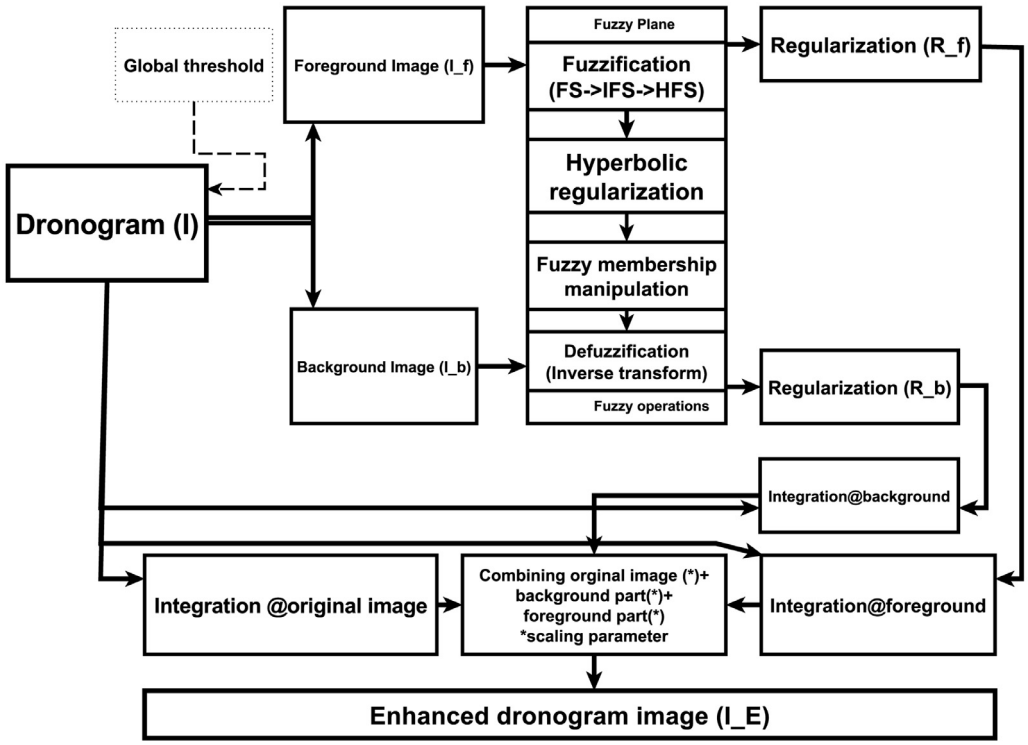

Fig. 1. Schematic diagram of the proposed DIEM model.

1. Compute the global threshold θ from whole image ($\mathbf{I}$) as,

$$\theta = \mu_I + \cdot(\mathbf{I}_{\max})\left[\frac{\mathbf{I}_{\max} - \mathbf{I}_{\min}}{n_b \cdot (\mathbf{I}_{\max} + \mathbf{I}_{\min})}\right]$$

   where, $\mathbf{I}_{\max}$ and $\mathbf{I}_{\min}$ represent the maximum, minimum intensity values of the dronogram ($\mathbf{I}$), respectively. μ_I is the mean of original image $\mathbf{I}$ and n_b bit level e.g. for 8-bit image, $n_b = 8$.
2. Fragment the dronogram ($\mathbf{I}$) using θ. This threshold twofolds $\mathbf{I}$ into foreground and background pixels such as $\mathbf{I}_f$ which puts together all pixels with intensity values $\mathbf{I} \geq \theta$, and $\mathbf{I}_b$ having all pixels with intensity values $\mathbf{I} < \theta$.
3. Compute the average intensity values μ_{I_f} and μ_{I_b} of all the pixels involved in $\mathbf{I}_f$ and $\mathbf{I}_b$, individually.
4. Calculate the mean threshold value $\hat{\theta}$ from foreground (μ_{I_f}) and background (μ_{I_b}) images as $\left[\hat{\theta} = \frac{\mu_{I_f} + \mu_{I_b}}{2}\right]$.
5. Update $\theta = \theta - \hat{\theta}$.
6. Repeat Steps (2) through (5) if $|\theta - \hat{\theta}| > \epsilon$ and set $\theta = \hat{\theta}$. Otherwise, make it as the final segmentation threshold θ. Here ϵ is a predefined parametric value set to $\epsilon = 0.005$ in DIEM.

Practically, for the original low-contrast (under-exposure) image, the pixel intensity distribution (illumination) in the background is darker. On the other hand, the pixel intensity distribution (illumination) in the foreground is brighter. But for an enhanced image, the black-white ratio (pixel intensity distribution) in background and foreground is stable and normalized [4,6,19]. Fig. 3(a)–(c) show the original under-exposure drone image, the background image, the foreground image, respectively.

3.3. Image fuzzification

To determine the exact fuzzy membership for foreground and background images, we use restricted equivalent relation (REF) with fuzzy decision theory [4,29]. Let $\mu_o(x) \in \mathbb{R}$ be an objective function, then the membership function is defined by two real valued functions such as $\phi_1 \in \mathbb{R}$ and $\phi_2 \in \mathbb{R}$ given below:

$$\mu_o(x, y) = \phi_1^{-1}\left(1 - \sqrt{1 - \phi_2^2(x) - \phi_2^2(y)}\right) \tag{20}$$

To constrain $\mu_C(x)$ function on the basis of Eq. (20), it is characterized by the membership function as

$$\mu_C(x, y) = \phi_2^{-1}(1 + \phi_1(x) \cdot \phi_2(y) - \zeta)^{-1}, \quad 0 \leq \zeta \leq 1 \tag{21}$$

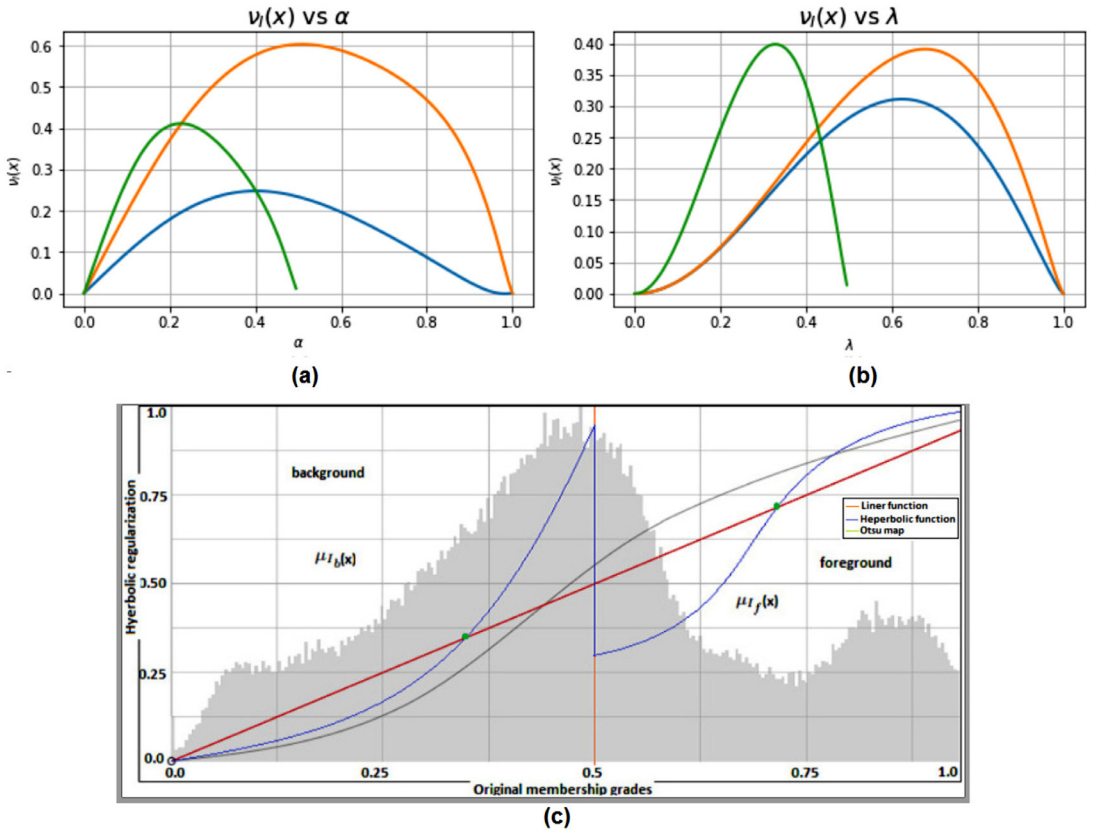

Fig. 2. Plots for (a)–(b) variation of membership grades $\nu_A(x)$ with parameters α and λ and (c) variation between the original and hyperbolic regularization.

where, ϕ_1, ϕ_2 and their inverse ϕ_1^{-1} can be written as follows:

$$\phi_1(x) = e^{(\alpha x^2 - 1)} - 1 \tag{22}$$

$$\phi_1^{-1} = \sqrt{\frac{1}{\alpha}\log(1+x)} \tag{23}$$

$$\phi_2(x) = x, \;\; \phi_2^{-1} = x^{-1} \tag{24}$$

Using Eq. (22) in Eq. (20), after simplification, we have

$$\mu_O(x,y) = \left(\sqrt{\frac{x}{\alpha}\log(1+x)}\right) \cdot \left(1 - \sqrt{1 - x^2 - y^2}\right) \tag{25}$$

Then, the membership function μ_C of the decision is given as

$$\mu_C(x,y) = \left(1 + y\left(x \cdot e^{(\alpha x^2 - 1)} - 1\right) - \zeta\right)^{-1}, \quad 0 \le \zeta \le 1 \tag{26}$$

By using Eqs. (25) and (26), we have

$$\mu_D(x,y) = 1 - \mu_O(x,y) \wedge \mu_C(x,y) \quad \forall x, y \le \zeta \in \mathbf{X} \tag{27}$$

$$\mu_D(x,y) = 1 - \mu_O(x,y) \vee \mu_C(x,y) \quad \forall x, y \ge \zeta \in \mathbf{X} \tag{28}$$

Applying Eqs. (27) and (28), the adjusted fuzzification for the foreground area μ_D^A can be expressed as,

$$\mu_D^A(x, m_A) = 1 - \mu_O(x, m_A) \wedge \mu_C(x, m_A)$$

$$m_A = \frac{1}{n_A}\sum_{i=0}^{n_A}\frac{\mu_A(x_i)}{x_i} \tag{29}$$

Similarly, the adjusted fuzzification for the background area μ_D^B is given by

$$\mu_D^B(x, m_B) = 1 - \mu_O(x, m_B) \vee \mu_C(x, m_B)$$
$$m_B = \frac{1}{n_B}\sum_{i=0}^{n_B}\frac{\mu_B(x_i)}{x_i} \tag{30}$$

where, m_A and m_B are the mean adjusted membership grades of foreground and background areas, respectively.

The fuzzy membership value of a pixel quantifies the grade of belongingness to the foreground or background area in an image. Hence, it is meaningful to split an image into foreground and background areas for contrast enhancement. For a given pixel belonging to a foreground or background area in an image with threshold θ, its membership grade is given as (from Eqs. (29) and (30))

$$\mu_A^l(x, m_A) = 1 - \mu_O^l(x, m_A) \wedge \mu_C^l(x, m_A) \tag{31}$$

$$\mu_D^l(x, m_B) = 1 - \mu_O^l(x, m_B) \vee \mu_C^l(x, m_B) \tag{32}$$

Fig. 2(c) shows the histogram of an image with a local area of grey levels. For source image, we have separated the image area into components **A** and **B**, where component **A** be related to component **B** in the fuzzy membership plane. The proposed model measures the divergence between components **A** and **B** by the hesitant score i.e., 0.3231. Typically, we have found that the intuitionistic fuzzy divergence is considered as 0.85 [1].

After that, we use the pixel value x_{ij} at point (i, j) in the foreground/background fuzzy hesitant image $h_{\mathcal{A}}/h_{\mathcal{B}}$ as defined by Eqs. (17) and (18) to replace the variable x by $\pi(x)$, and the average gray value of the block (viz., m_A/m_B) in Eqs. (31) and(32). Then, the final fuzzy membership grades for the foreground area $h_{\mathcal{A}}$ can be expressed as,

$$\mu_A^l(\pi_{\mathcal{A}}(x), m_A) = 1 - \mu_O(\pi_{\mathcal{A}}(x), m_A) \wedge \mu_C(\pi_{\mathcal{A}}(x), m_A)$$
$$\pi_A(x) = [1 - \mu_A(x) - \nu_A(x)] \tag{33}$$

Similarly, the final fuzzy membership grades for the background area at space $h_{\mathcal{B}}$ are,

$$\mu_B^l(\pi_B(x), m_B) = 1 - \mu_O(\pi_B(x), m_B) \vee \mu_C(\pi_B(x), m_B)$$
$$\pi_B(x) = [1 - \mu_B(x) - \nu_B(x)] \tag{34}$$

According to IFS [1], we construct two sets such as $\mu_{\mathbf{A}}^{IFS}(x)$, $\mu_{\mathbf{B}}^{IFS}(x)$ from $\mu_{\mathbf{A}}^{FS}(x)$, $\mu_{\mathbf{B}}^{FS}(x)$ by applying Eq. (7) individually. $\mu_{\mathbf{A}}^{IFS}$ and $\mu_{\mathbf{B}}^{IFS}$ are formed by fuzzy membership degree μ, hesitation degree π and non-membership degree ν of $\mu_{\mathbf{A}}^{IFS}$ and $\mu_{\mathbf{B}}^{IFS}$ by applying Eq. (8). To determine the membership degree of $\mu_{\mathbf{A}}^{IFS}(x)$ for each pixel to foreground region, we formulate following expression:

$$\mu_{\mathcal{A}}^{\mathbf{IFS}}(x) = \{\langle \mu_A(x), \pi_A(x), \nu_A(x)\rangle | x \in \mathbf{X}\} \tag{35}$$

Hence, we define the membership degree of $\mu_{\mathbf{B}}^{IFS}(x)$ for each pixel to background region, by the following expression

$$\mu_{\mathcal{B}}^{\mathbf{IFS}}(x) = \{\langle \mu_B(x), \pi_B(x), \nu_B(x)\rangle | x \in \mathbf{X}\} \tag{36}$$

where, $\mu_A(x)$ and $\mu_B(x)$ denote the intuitionistic fuzzy membership of sets **A** and **B** for image **I**. The hesitation degree and non-membership degree are initially estimated by using Eqs. (7) and (8) for both of them. Finally, the intuitionistic fuzzy membership grades for **A** and **B** are achieved as follows:

$$\mu_A^a(x) = [\mu_A(x) + \pi_A(x)] \tag{37}$$

$$\mu_B^b(x) = [\mu_B(x) + \pi_B(x)] \tag{38}$$

The membership grades of the foreground intuitionistic fuzzy hesitant set belongs to bright pixels in the foreground area, whereas the membership grades of background belongs to dim pixels in foreground area. The relationship of intuitionistic fuzzy membership grade $\nu(x)$ and hesitant grade $\pi(x)$ with two parameters α and λ are shown in Fig. 2(a) and (b).

3.4. Hyperbolic regularization scheme

In this work, we generate suitable membership grades for better contrast using the following hyperbolic regularization function [29,33]:

$$\mathbf{d}_h(x, a) = \ln(\chi(x, a)) + \sqrt{1 - \chi(x, a)^2}$$

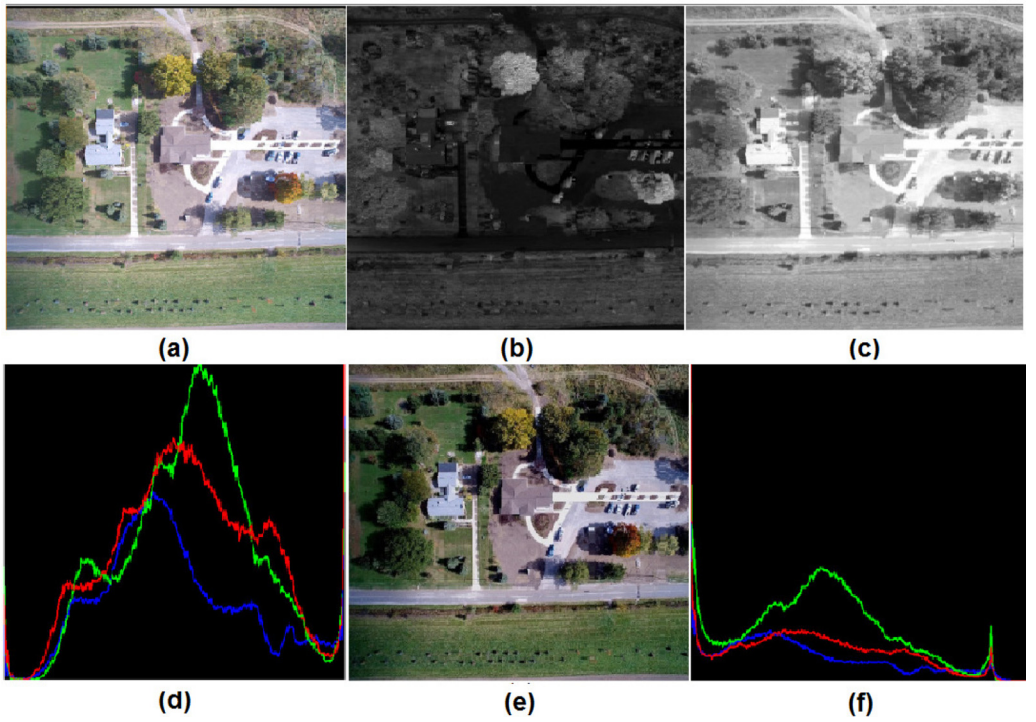

Fig. 3. Showing the histograms of a dronogram (a), the corresponding background area (black) (b), foreground area (white) (c) histogram before enhance, (d) enhanced result and (e) histogram after enhance.

$$\chi(x,a) = \left[1 - \frac{\left||x-a|\right|_2^2}{2xa}\right] \tag{39}$$

where, $\left||x-a|\right|_2^2$ denotes the Euclidean distance in $\mathbb{R}^2$ between two points x and a (fixed point). In addition, $\chi(x,a) = 0$ if $x = a$ and $\forall x \in \mathcal{X}$ with $0 \le x \le 1$, $\chi(x, a)$ always fulfils $0 \le \chi(x, a) \le 1$ [5,33]. The hyperbolic regularization procedure is adopted to expand the liking of the pixels whose intensity levels are closer to the average gray of the foreground (object) to the background of an image. Similarly, the hyperbolic regularization is used to reduce the liking of the pixels to the average gray of the foreground (object) or background area for those pixels whose gray levels are wider from the average gray of the foreground (object) or the background area of the image [6,28–30].

The hyperbolic regularization for a foreground area ($\mu^a_{\mathcal{A}}(x)$) using Eq. (39) is given as:

$$\hat{\mu}^a_{\mathcal{A}}(x) = \begin{cases} \mu^a_{\mathcal{A}}(\theta) - \mathbf{d}^a_{\mathcal{A}_h}(\mu^a_{\mathcal{A}}(x), \mu^a_{\mathcal{A}}(\theta)) \cdot \left(\sqrt{\mathcal{S}^a_{\mathcal{A}}(\cdot) + \mathcal{H}^a_{\mathcal{AB}}(\cdot)\left(\mu^a_{\mathcal{A}}(\theta)^2 - \mu^a_{\mathcal{A}}(x)^2\right)}\right) \\ \text{if } \mu^a_{\mathcal{A}_{\min}} \le \mu^a_{\mathcal{A}}(x) \le \mu^a_{\mathcal{A}}(\theta) \\ \mu^a_{\mathcal{A}}(\theta) - \mathbf{d}^a_{\mathcal{A}_h}(\mu^a_{\mathcal{A}}(x), \mu^a_{\mathcal{A}}(\theta)) \cdot \sqrt{\mathcal{S}^a_{\mathcal{A}}(\cdot) + \mathcal{H}^a_{\mathcal{AB}}(\cdot)\left(\left(1-\mu^a_{\mathcal{A}}(\theta)\right)^2 - \left(1-\mu^a_{\mathcal{A}}(x)\right)^2\right)} \\ \text{if } \mu^a_{\mathcal{A}}(\theta) \le \mu^a_{\mathcal{A}}(x) \le \mu^a_{\mathcal{A}_{\max}} \end{cases} \tag{40}$$

$$\text{where } \mu^a_{\mathcal{A}}(\theta) = \frac{1}{\alpha}\left[\frac{\left(1-\left(\mu^a_{\mathcal{A}_{\min}}\right)^{\alpha}\right)^k}{1+\lambda\left(\mu^a_{\mathcal{A}_{\max}}\right)^{\alpha}}\right],\ \alpha > 0\ \lambda > 0$$

Similarly, the hyperbolic regularization for a background area ($\mu^b_{\mathcal{B}}(x)$) by applying Eq. (39) is determined as:

$$\hat{\mu}^b_{\mathcal{B}}(x) = \begin{cases} \mu^b_{\mathcal{B}}(\theta) - \mathbf{d}^b_{\mathcal{B}_h}\left(\mu^b_{\mathcal{B}}(x), \mu^b_{\mathcal{B}}(\theta)\right) \cdot \left(\sqrt{\mathcal{S}^b_{\mathcal{B}}(\cdot) + \mathcal{H}^b_{\mathcal{AB}}(\cdot)\left(\mu^b_{\mathcal{B}}(\theta)^2 - \mu^b_{\mathcal{B}}(x)^2\right)}\right) \\ \text{if } \mu^b_{\mathcal{B}_{\min}} \le \mu^b_{\mathcal{B}}(x) \le \mu^b_{\mathcal{B}}(\theta) \\ \mu^b_{\mathcal{B}}(\theta) - \mathbf{d}^b_{\mathcal{B}_h}\left(\mu^b_{\mathcal{B}}(x), \mu^b_{\mathcal{B}}(\theta)\right) \cdot \sqrt{\mathcal{S}^b_{\mathcal{B}}(\cdot) + \mathcal{H}^b_{\mathcal{AB}}(\cdot)\left(\left(1-\mu^f_{\mathcal{B}}(\theta)\right)^2 - \left(1-\mu^b_{\mathcal{B}}(x)\right)^2\right)} \\ \text{if } \mu^b_{\mathcal{B}}(\theta) \le \mu^b_{\mathcal{B}}(x) \le \mu^b_{\mathcal{B}_{\max}} \end{cases} \tag{41}$$

$$\text{where } \mu^b_{\mathcal{B}}(\theta) = \frac{1}{\alpha}\left[\frac{\left(1-\left(\mu^b_{\mathcal{B}_{\min}}\right)^{\alpha}\right)^{k}}{1+\lambda\left(\mu^b_{\mathcal{B}_{\max}}\right)^{\alpha}}\right],\ \alpha>0\ \lambda>0$$

where, $\hat{\mu}^a_{\mathcal{A}}(x)$ and $\hat{\mu}^b_{\mathcal{B}}(x)$ denote the hyperbolic regularized membership grades of each point in $\mu^a_{\mathcal{A}}(x)$ and $\mu^b_{\mathcal{B}}(x)$ at the fuzzy hyperbolic space. The threshold θ is calculated by an iterative approach from, $\mu^a_{\mathcal{A}_{\min}}$ and $\mu^a_{\mathcal{A}_{\max}}$, which represent the minimum and maximum membership grades of the foreground area $(\mu^a_{\mathcal{A}}(x))$. $\mu^b_{\mathcal{B}_{\min}}$ and $\mu^b_{\mathcal{B}_{\max}}$ stand for the minimum and maximum membership grades of the background area in the fuzzy plane. $\mathcal{H}_{\mathcal{AB}}(\cdot)$ is the normalized Hamming hesitant fuzzy distance between two IHFSs $\mu^a_{\mathcal{A}}(x)$ and $\mu^b_{\mathcal{B}}(x)$.

Fig. 2(c) shows the relationship between a linear and a hyperbolic function where the red, blue and green color denote the linear curve, normal hyperbolic function and the suggested hyperboloid function (the crossover point on reference line is set as 0.5). The vertical line is the partition plot between the foreground and background areas. For example, we take two point such $x = 0.4$ and reference cross point $a = 0.5$. According to Eq. (39), we achieve new hyperbolic regularized membership $(= 0.4381)$. It is obvious that the new point is more close to a reference point $(a = 0.5)$ than a previous point $(x = 0.4)$. Similarly, for two-points $a = 0.5, x = 0.4$ in [6,30], we have found a new membership value of $(x = 0.4173)$ that is less than the proposed approach.

3.5. Image defuzzification

We improve and modify each membership degree in terms of hyperbolic regularization approach for foreground $(\mu^a_{\mathcal{A}}(x))$ and background $(\mu^b_{\mathcal{B}}(x))$ via the transformation of hesitant intuitionistic fuzzy image (HIFI) $(\mathcal{I}_{(\alpha,\lambda)})$ in the fuzzy plane. In the defuzzification stage, the hyperbolic regularized membership grades at the fuzzy plane are converted into the image plane through defuzzification operation. According to Eqs. (7)–(11) and Eqs. (40) and(41) along with mathematical simplification, the defuzzification for the foreground area is achieved as follows:

$$\mathbf{R}_a(x) = \left[\mathbf{I}_{L_{\max}} - \left(\mathbf{I}_{L_{\max}} - \mathbf{I}_{L_{\min}}\right)\left(\frac{\left(1-\hat{\mu}^a_{\mathcal{A}}(x)\right)}{\left(2k+\lambda\hat{\mu}^a_{\mathcal{A}}(x)\right)}\right)\right] \tag{42}$$

On the other hand, the defuzzification for the background area is achieved as follows:

$$\mathbf{R}_b(x) = \left[\mathbf{I}_{L_{\max}} - \left(\mathbf{I}_{L_{\max}} - \mathbf{I}_{L_{\min}}\right)\left(\frac{\left(1-\hat{\mu}^b_{\mathcal{B}}(x)\right)}{\left(2k+\lambda\hat{\mu}^b_{\mathcal{B}}(x)\right)}\right)\right] \tag{43}$$

where, $\mathbf{R}_a$ and $\mathbf{R}_b$ represent the fresh gray value at all the pixels in foreground and background areas, and $\mathbf{I}_{L_{\min}}$ and $\mathbf{I}_{L_{\max}}$ indicate the minimum and maximum gray values $\mathbf{L}$ of the original dronogram $\mathbf{I}$, respectively. For example, Fig. 3(d)–(f) depicts the histogram before and after enhancement.

3.6. Enhanced image reconstruction from image partitions

To achieve enhanced results, we combine the normalized foreground $(\mathbf{I}_f)$, background $(\mathbf{I}_b)$ and original $(\mathbf{I})$ images in terms of certain arithmetic operators (such as division, dot product, etc.). We apply the multiplication $(\cdot)$ and addition $(+)$ arithmetic operators for integrating fuzzy data in **DIEM** to achieve the desired enhancement. In this work, we use point wise computation by the operator addition $(+)$ and multiplication $(\cdot)$ in **DIEM**. After that, the enhanced result $(\mathbf{I}_E)$ is obtained the by following formula:

$$\begin{aligned}
\mathbf{I}_E(x) &= ((\kappa_o \cdot \mathbf{I}_0(x)) + (\kappa_b \cdot \mathbf{R}_b(x)) + (\kappa_a \cdot \mathbf{R}_a(x)))\\
\mathbf{R}_b(x) &= \Upsilon(\Xi(\Phi(\Lambda(\mathbf{I}(x)))))\\
\mathbf{R}_a(x) &= \Upsilon(\Xi(\Phi(\Lambda(\mathbf{I}(x)))))
\end{aligned} \tag{44}$$

where, κ_o, κ_b and κ_a are the scaling parameters for original, background and foreground images, respectively. $\mathbf{I}(x)$ denotes the input dronogram. On the other hand, the functions Λ, Φ, Ξ, and Υ represent the fuzzification, hyperbolic regularization, defuzzification, and normalization operations applied on $\mathbf{I}(x)$ orderly, and $\cdot$ denotes the simple multiplication operation.

For a given original under-exposed (dim) image, typically the histogram curve is nearly close to the left of the histogram abscissa and for a over-exposed (high-contrast) image, the corresponding histogram curve is more close to the right of the histogram abscissa. However, for an enhanced image, the histogram curve mainly fits in left to right of the histogram abscissa (Fig. 2). Fig. 3(d)–(f) show the histograms of the under-exposed, enhanced drone image, and Fig. 3(a) show the source image, respectively. From Fig. 3(d)–(f), we can observe that the peak of the histogram curve for the enhanced image is flatter from left to right abscissa in the histogram. The pseudo code of DIEM is described in Algorithm 1.

Algorithm 1 Pseudo code of DIEM.

Require: Image data $X(x, y) \in I \in \mathbb{Z}^{(M\times N)}$;
Initialize: α, λ, $\kappa = (1 + 1/\alpha)$, $x_L^{\min}$, θ, $n = M \times N$ and $x_L^{\max}$;
Output: **R**, the enhanced version of **I**;

Begin

Step 1. Load data matrix **X** ;

Step 2. Compute:

$$\mu_X(x_i) = \left[\frac{\mathbf{x}_i - x_L^{\min}}{x_L^{\max} - \mathbf{x}_i}\right], i = 1, 2, \ldots, \mathbf{N};$$

Step 3. Compute:

$$\mathcal{X}_{(\alpha,\lambda)} = \left\{\left\langle x, \mu_X(x), \left[\frac{\left(1 - \mu_X(x)^\alpha\right)^k}{1 + \lambda\mu_X(x)^\alpha}\right]\right\rangle : x \in \mathcal{X}\right\}$$

Step 4. Compute:

$$\pi_{\mathcal{X}}(x) = \left\{1 - \mu_X(x) - \left[\frac{\left(1 - \mu_X(x)^\alpha\right)^k}{1 + \lambda\mu_X(x)^\alpha}\right]\right\}$$

and calculate

$$\nu_{\mathcal{X}}(x) = \left\{\left(1 - \mu_X(x)^\alpha\right)^k\right\}$$

Step 5. Compute:

$$\mathcal{S}_{HS}^{\mathcal{X}}(\cdot) = \frac{1}{n}\sum_{i=1}^{n}\left[\frac{1}{\mathbf{c}_{x_i}}\sum_{j=1}^{\mathbf{c}_{x_i}} h_{\mathcal{X}}^{\sigma(j)}(x_i)\right];$$

Step 6. Compute:

$$\hat{\mu}_{\mathcal{X}}^* = \mu_{\mathcal{X}}^*(\theta) - \mathbf{d}_{\mathcal{X}_h}^*(\mu_{\mathcal{X}}^*(x), \mu_{\mathcal{X}}^*(\theta))$$

$$\text{where}\mu_{\mathcal{X}}^*(\theta) = \frac{1}{\alpha}\left[\frac{\left(1 - \left(\mu_{\mathcal{X}_{\min}}^*\right)^\alpha\right)^k}{1 + \lambda\left(\mu_{\mathcal{X}_{\max}}^*\right)^\alpha}\right], \alpha > 0\lambda > 0;$$

Step 7. Defuzzify with (44) to compute

$$\mathbf{R}_*(x) = \left[\mathbf{I}_L^{\max} - \left(\mathbf{I}_L^{\max} - \mathbf{I}_L^{\min}\right)\left(\frac{\left(1 - \hat{\mu}_{\mathcal{X}}^*(x)\right)}{\left(2k + \lambda\hat{\mu}_{\mathcal{X}}^*(x)\right)}\right)\right];$$

Step 8. Calculate **R**;

End

4. Experiments results and analysis

In this section, we discuss the performance measures and efficiency of the proposed **DIEM** method in comparison to several performance measure metrics and baseline methods.

4.1. Benchmark data

The validation of the suggested scheme is tested on a large drone image database and the test data sets are taken from authorized websites [44]. In simulation, we have selected a set of RGB colour images with size 512×512 pixels with 8 bits-per-pixel. The images selected are not clear and are either lowly illuminated or blurred. We have used more than 100 images to validate the enhancement performance of the proposed DIEM method. As an example, some original sample images (viz. âGarfield Parkâ, âToledoâ, âLewisâ) are shown in Fig. 4 (1st column).

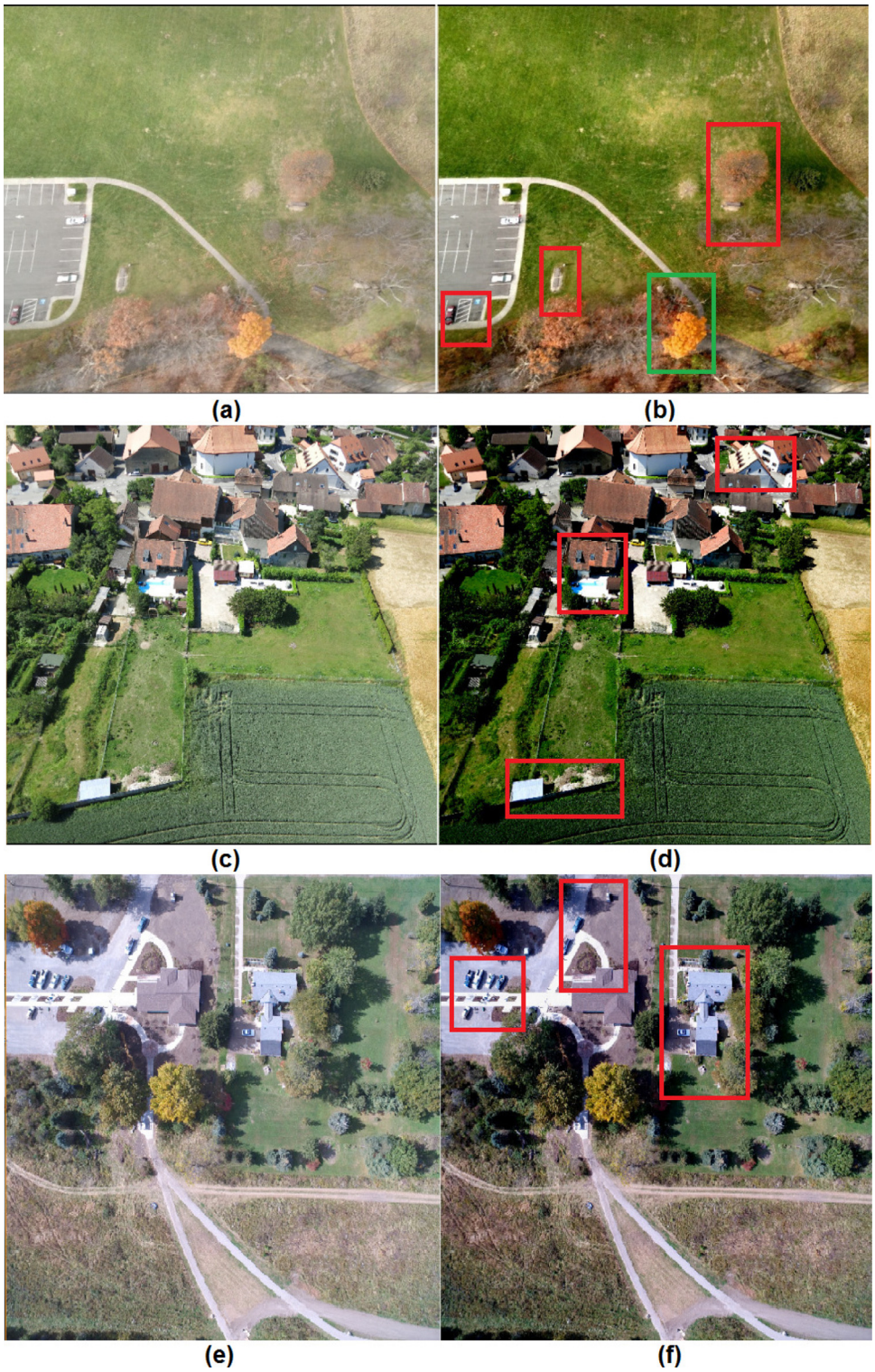

Fig. 4. Visual enhancement (ODM datasets: Garfield Park, Toledo, Lewis): (a) the original image(4000×3000)(1st-column) (b) enhanced by the DIEM(2nd-column).

Table 1
Statistical based quantitative evaluation of baseline methods.

Image	Method	MAE	EMEE	AME	AMEE
	PLE	0.131	1.153	113.2	0.381
	FSE	0.132	1.212	113.7	0.382
Fig. (5)	MIEF	0.131	1.338	113.8	0.383
	RDH	0.125	1.421	114.1	0.391
	DIEM	**0.124**	**1.503**	**114.7**	**0.404**
	PLE	0.141	1.181	115.1	0.394
	FSE	0.142	1.238	115.3	0.396
Fig. (6)	MIEF	0.135	1.329	115.6	0.398
	RDH	0.130	1.427	115.7	0.407
	DIEM	**0.1265**	**1.510**	**116.9**	**0.413**
	PLE	0.137	1.185	113.5	0.388
	FSE	0.136	1.227	113.8	0.3897
Fig. (7)	MIEF	0.134	1.340	113.9	0.390
	RDH	0.131	1.441	114.10	0.393
	DIEM	**0.129**	**1.591**	**114.8**	**0.401**

4.2. Performance metrics

The quantitative evaluation of contrast enhancement techniques is a challenging task. There exists no universally accepted quantitative and qualitative evaluation methods for the exact measure of enhancement of individual resultant images. All performance measuring schemes are not able to determine the quality of visual contrast of an enhanced image in uniform situations.

However, to validate the effectiveness and quality of image enhancement, we have used different performance metrics such as mean absolute error (MAE) [13,36], linear index of fuzziness (LIF) [14,22], Weber-law-based contrast measure (EMEE) [14], Michelson law measure of enhancement (AME) [13,36], Michelson law measure of enhancement by entropy (AMEE) [13,36], universal quality index (UQI) [14], Structural Similarity index measure (SSIM) [13,14,35,36], fuzzy quality index (Q/FS) [13,14,36] and Intuitionistic fuzzy quality index (Q/IFS) [13,14] to assess the efficiency of DIEM. The higher values of all the aforementioned metrics indicate better enhancement except MAE and LIF [14,36]. MAE, EMEE, AME and AMEE are conventional statistical based metrics whereas LI, UQI, SSIM, Q/FS and Q/IFS are image quality measurement metrics.

4.3. Enhancement analysis

In this section, we discuss the performance of the enhancement task. Both the quantitative assessment as well as qualitative analysis with comparative study have been explored in this treatment.

4.3.1. Quantitative evaluation

In quantitative evaluation, we have tested the DIEM method on one hundred drone images taken from 'OpenDroneMapâ (ODM) [44] and compared with four state-of-the-art enhancement methods in this study. The selected four baseline methods are 'Parameterized logarithmic framework for image enhancement' (**PLF**) by Panetta *et al.* [25], 'A novel image enhancement method using fuzzy Sure entropy'(**FSE**) by Li et al. [19], 'A novel reversible data hiding method with image contrast enhancement' (**RDH**) by H.T. Wu *et al.* [37], and 'Mammogram Enhancement using Intuitionistic Fuzzy Sets' (**MEIF**) by Deng et al. [6]. FSE and MEIF are scheduled for completion with default parameters, as recommended in their own papers. The quantitative and visual assessment of the enhanced images by the different baseline methods are executed to analyze the overall performance. The **DIEM** method is devised on **Anaconda Python (vs.-3.6)** programming language on 64-bit **Ubuntu 18.04 LTS Linux system** with Intel Core i3 CPU-3.5 GHz and 16-GB RAM.

For the purpose of quantitative description, Tables 1 and 2 show the metrics for each enhanced results by all the baseline methods as shown in Figs. 5–7, respectively. It is pointed out that the proposed DIEM method produces the lowest MAE and LIF than other baseline methods which indicate that DIEM provides better-enhanced images. Performance is further computed by using UQI, SSIM, Q/FS, Q/IFS for each test. Tables 1 and 2 provide the MAE, UQI, and SSIM, Q/FS, and Q/IFS indices for all the methods. Lower MAE, LIF and a higher UQI, SSIM, Q/FS, and Q/IFS indicate the best contrast. It is important to use more quantitative assessment for exact performance evaluation of DIEM. Hence, we have used some popular statistical metrics such as EMEE, AME and AMEE in this work. The estimated results of EMEE, AME and AMEE are provided in Table 1. DIEM has achieved higher EMEE, AME and AMEE values than the baseline methods which indicates that DIEM more efficient to enhance drone image.

Similarly, the universal quality index (UQI) and structural similarity (SSIM) as well Q/FS, and Q/IFS are measured for all the baseline methods and DIEM. Higher UQI values specify that the contrast is improved. On the other hand, for better structural similarity between the source and enhanced images, the SSIM value is very close to 1. The estimated values of all the methods are listed in Table 2, where metric values achieved by DIEM are listed in boldface. It is important to note that baseline methods and DIEM yield different results for the enhanced drone images. Tables 1 and 2 suggest that DIEM

Table 2
Image quality based quantitative evaluation of baseline methods.

Image	Method	LI	UQI	SSIM	Q/FS	Q/IFS
	PLE	0.213	0.97856	0.96456	0.83942	0.83389
	FSE	0.215	0.97855	0.96827	0.84019	0.84369
Fig. 5	MIEF	0.211	0.97959	0.97022	0.84238	0.85950
	RDH	0.212	0.98979	0.97614	0.84476	0.86808
	DIEM	**0.209**	**0.99953**	**0.98809**	**0.84911**	**0.88737**
	PLE	0.221	0.98614	0.97024	0.85109	0.85143
	FSE	0.220	0.98627	0.97281	0.85328	0.85487
Fig. 6	0.218	MIEF	0.98738	0.98263	0.85671	0.86661
	RDH	0.213	0.99819	0.98509	0.85794	0.87812
	DIEM	**0.210**	**0.99985**	**0.99758**	**0.86033**	**0.88908**
	PLE	0.216	0.98174	0.97684	0.83911	0.83861
	FSE	0.215	0.98298	0.97709	0.84128	0.84572
Fig. 7	MIEF	0.211	0.98303	0.97983	0.84303	0.85013
	RDH	0.208	0.98326	0.98292	0.84501	0.86279
	DIEM	**0.203**	**0.99651**	**0.99758**	**0.84972**	**0.87058**

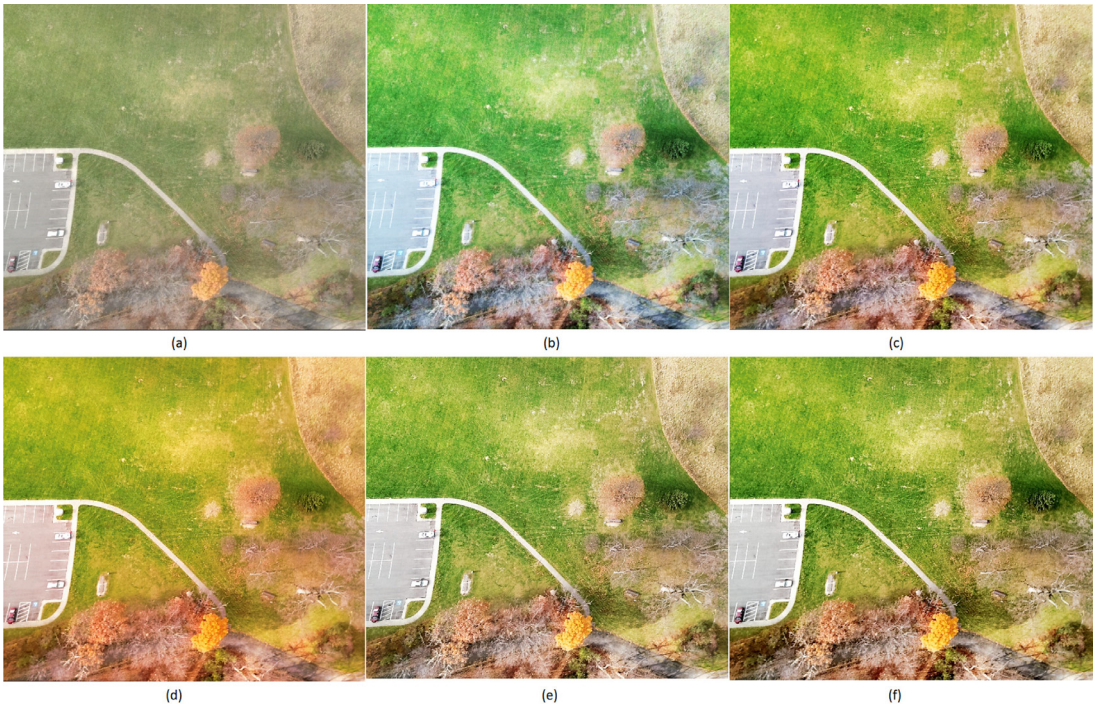

Fig. 5. Comparative enhanced results of baseline methods: (a) the original image, (b) PLF method, (c) FSE method, (d) MEIF method, (e) RDH method, and, (f) DIEM method.

for Garfield drone image gives the best visual quality score with 0.1245, 0.2098, 1.5039, 114.7139, 0.4039, 0.99953, 0.98809, 0.84911, and 0.88737. However, PLF obtains slightly poor visual quality score with 0.1315, 0.2136,1.1538, 113.2538, 0.3818, 0.97856, 0.96456, 0.83942 and 0.83389, respectively. We have observed from Tables 1 and 2 that DIEM is better than other baseline methods with respect to MAE, LIF, EMEE, AME, AMEE, UQI, SSIM, Q/FS, and Q/IFS.

Furthermore, Tables 1 and 2 represent the contrast measures for 'Toledo' data as shown in Figs. 6 and 7 obtained with the baseline methods. For two groups of 'Toledo' drone images, the DIEM method obtains MAE, LIF, EMEE, AME, AMEE, UQI, SSIM, FSQI, and IFSQI values with scores of 0.1265, 0.2108, 1.5107, 116.9181, 0.4135, 0.99985, 0.99758, 0.86033, and 0.88908 for first Toledo (Fig. 7(f)) and scores of 0.1295, 0.2031, 1.5918, 114.8107, 0.4006, 0.99651, 0.99758, 0.84972, and 0.87058 for last Toledo (Fig. 7(f)), respectively. The above objective measures (MAE, LIF, EMEE, AME, AMEE, UQI, SSIM, FSQI, and IFSQI) indicate DIEM has improved the pictorial quality compared to the baseline methods. So, the enhanced results obtained using the proposed DIEM method are almost accurate and useful in recognizing different types of scanning target objects accurately. This will provide assistance to user to precept the target objects clearly.

Fig. 6. Comparative enhanced results of baseline methods: (a) the original image, (b) PLF method, (c) FSE method, (d) MEIF method, (e) RDH method, and, (f) DIEM method.

Fig. 7. Comparative enhanced results of baseline methods: (a) the original image, (b) PLF method, (c) FSE method, (d) MEIF method, (e) RDH method, and, (f) DIEM method.

4.3.2. Qualitative analysis

Various enhanced approaches have been used to assess and analyze the enhancement results in the literature. To visually improve an underexposed (very low-light) image for exact discrimination of the object boundaries in ROIs, we have suggested DIEM in this study. We have simulated the designed method with a set of raw drone data in this experiment. For example, Fig. 4(a) demonstrates dronograms with car parking region, where few cars are found present. The boundaries between the green region and park along the parking road are much blurry in the original test data *Garfield* of **OpenDroneMap (ODM)**. From the enhanced results obtained by DIEM, it is clear that dim regions are more clear and easy to be discernible without any effort. The car parking region is highlighted in the **Garfield** data by square and its clear appearance assists for better understanding and visualization of the target objects like cars, trees under the green field compared with the original image.

Four ground truth dronograms of *OpenDroneMap(ODM)* such as *Garfield* (Fig. 5(a)), *Toledo* (Fig. 4)(b), (Fig. 6)(a) and *Lewis* (Fig. 7(a) contain different objects (car, trees, roads houses and etc.) which are visually slightly unclear as well as the locations of target objects and their morphological details seem to be obscure in the original images. However, after application of the proposed DIEM technique, those differences are improved in the enhanced results as shown in Fig. 4(b)–(f). It is observed that deformities in ROI can be easily identified by DIEM. As a result, we can use DIEM for object recognition and to discriminate the proper location of object positions under scanned dronograms. Also, it is helpful to differentiate and highlight the deformities of ROI in dronograms.

4.4. Regions of interest

When a user observes a digitized dronogram, he or she usually observes the spatial positions of the target objects and describes their morphological details with a ROI. If an enhanced version of ROI is present alongside the original image, the user can switch between the original dronogram and the automatically enhanced views for comparison. Accordingly, he/she can easily describe any new details or features which are manifested to him or her that can even identify some activity findings in dronograms.

Three dronograms (viz. 'Garfield Park, 'Toledo', 'Lewis') with target and/or ROI are displayed in Fig. 4, where the color box covers the locations of the ROI. The red rectangles indicate the ROIs and highlighting target objects as shown in Fig. 4(b),(d),(f). We can see that the contrast of target object is distinct in the enhanced results achieved by the DIEM method. It can be found that both the visual quality and contrast of the enhanced ROIs are much better than that of the original ones. To synchronously show enhanced target objects as well as normal object boundary, the enhanced ROIs are superimposed with the corresponding original dronograms, as shown in Fig. 4(a)–(f), where the red areas consisting of certain pixels denote the detected region and/or ROIs. These pixels are visually clear in enhanced ROIs and the edges are also refined well.

The detected image objects and/or ROIs are assessed by a drone expert majoring in the monitoring of a drone. He/She considers that the detected results are accurate reflections of target regions (viz. scanned object when drone monitoring) in dronograms. Moreover, these results facilitate to recognize and analysis further tasks. In results, the DIEM algorithm shows the improvement of the contrast as well as the visual quality of target regions. This proves that DIEM has potential for understanding the target object details and to identify the target ROIs by enhancing fine details in dronograms inducing the capability of the object detection task.

4.5. Comparisons with baseline methods

We have conducted three experiments to get considerably a more detailed qualitative assessment to investigate the effectiveness of DIEM to enhance drone raw images. At the end of each experiment, the objective measures are evaluated to ensure that the tracing of image objects can be easily achieved in the presence of image enhancement as compared to other baseline methods. The proposed DIEM method has been compared with recent state-of-the-art enhancement algorithms with large dronogram data sets [44]. As mentioned above, we use four well-known baseline methods for performance evaluation notationally expressed as PLF, FSE, MEIF and RDH, respectively. We have used the baseline methods with their suggested parameters in literature.

In the simulation, we have used benchmark color dronograms of size 512×512 pixels with 8 bits-per-pixel. To show enhancement performance of the DIEM algorithm, Fig. 5 shows the results for all the images, respectively. For all the test images, the enhanced results achieved by the baseline methods PLF, FSE, MEIF, RDH, and DIEM are shown in Figs. 5–7, respectively. For instance, the first selected 'Garfield park' drone image and the enhanced results obtained by the baseline methods are shown in Fig. 5 (a) (original drone image) and the remaining shown in Fig. 5 (b)–(f) are those obtained with PLF, FSE, MEIF, RDH, and DIEM methods, respectively. For the case of a low illuminated image, testing of color contrast improvement methods is a hard and challenging task. For example, the enhanced results obtained by the baseline methods and the proposed method are visually different. So, the purpose of defining an efficient algorithm in this study is to ensure highly informative visual content and significant illuminated images for better interpretation. From the results, we have observed that the visual improvement after the proposed DIEM enhancement method shown in Fig. 5(f) is almost better than the baseline methods in Fig. 5(b)–(e).

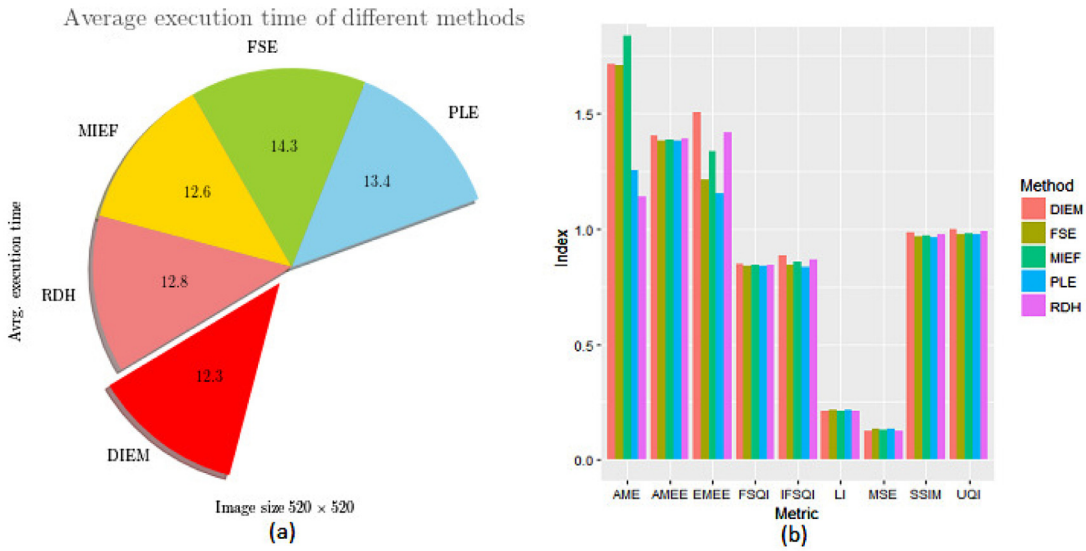

Fig. 8. Comparing results of baseline methods: (a) average run time (unit on sec.), (b) performance metric (average values).

In the second experiment, we have tested all the methods with the 'Lewis' drone image with size $512 \times 512 \times 3$. We have noted that all the baseline algorithms except PLF have slightly improved the visual quality in the resultant images as shown in Fig. 6(a)–(e), respectively. MEIF, RDH and DIEM have given better effect and thereby assist to distinguish the image objects for better understanding. However, MEIF and RDH produce over enhanced images than DIEM on the boundary regions of the image objects in the 'Lewis' dronogram as shown in Fig. 6(d) and (e). Perceptibly, PLF and FSE have generated artifacts at the edges of objects and provide a blurry view than the original ones. In contrast, DIEM not only improves the background of the image but also successfully achieves prominent boundary regions and sharp edges depicted in Fig. 6 (f). From Fig. 6(b)–(f), for all baseline methods, we have observed that the proposed DIEM method is better than the baseline methods due to its improved capability in producing clarity of distinct regions and better exposure on object details.

In the last test, we have selected another sample of the 'Lewis' drone image in this study. The enhanced results of all the baseline methods including DIEM are shown in Fig. 7(b)–(f), respectively. Compared to Fig. 7(a)–(f), the proposed method DIEM successfully improves the local contrast and visually sharpen boundary regions. We have also noted that the image details generated by PLF and FSE shown in Fig. 7(b),(c) fail to preserve the colour details. Moreover, the boundary regions are slightly blurred. The existing MEIF and RDH methods produce much brighter images but slight hazy effects on object boundary especially trees, cars and roads. In addition, the inner structures are not clearly visible. Fig. 7(a) is just an original image of the 'Lewis' drone dataset where the object regions (viz. houses, cars and roads) are not well visible. It is clear that the enhanced image after application of the proposed DIEM method (Fig. 7(e)) contains almost higher object details and is visually prominent to easily distinguish the scanned objects more accurately.

The computed performance metrics (viz., MAE, LIF, EMEE, AME, AMEE, UQI, SSIM, Q/FS, and Q/IFS) obtained with DIEM are presented in Tables 1 and 2 (listed in bold). These are also illustrated graphically in Fig. 8(b). It is seen that DIEM is well suited for the task of contrast enhancement. It observed that DIEM is statistically more distinct from all the baseline techniques in subjective and/or objective evaluation. Consequently, the quantitative and qualitative comparisons demonstrate that the proposed DIEM method provides better performance than the baseline methods. Thus it is beneficial for differentiating and highlighting objects in dronograms and assist in further operations in advanced image processing (e.g. object detection, classification and etc.). A lot of images in 'OpenDroneMap' (ODM) are complex enough for enhancement purposes as they contain small objects (viz., men, small trees.) in drone images. These images show better enhancements when considered for DIEM technique. This shows that the DIEM algorithm is good enough for such challenging cases in drone image enhancement.

In summary, the proposed DIEM method outperforms the baseline enhancement techniques as specified by the subjective and objective evaluations. The proposed DIEM method offers better contrast and visually true results mainly for tough-to-enhance drone images such as those underexposed with obscure images. Moreover, the stability and consistency of an enhancement algorithm are more important to perform a constant enhancement for all images, especially for the low illuminated cases. Our experiments can be summarized with the following observations:

1. Enhancing drone images to make them visually improved for better understanding of the relationships between different parts of the object regions in dronogram.
2. Visual enhancement is facilitated to differentiate and perceive target objects.
3. Enhancing drone images improves the view for high-fidelity objects.

Table 3
The execution time of baseline methods (s).

Computational time of the all enhancement methods on the CPU					
Image	PLE	FSE	MIEF	RDH	DIEM
Image 5	0.1392	0.1412	0.1253	0.1275	**0.1232**
Image 6	0.1329	0.1409	0.1261	0.1276	**0.1229**
Image 7	0.1308	0.1467	0.1252	0.1279	**0.1231**

4.6. Time complexity analysis

To compute the execution time, we carried out an extensive assessment with a larger drone database with image size 512×512. The average run time of the different baseline methods for each image is listed in Table 3. We use Python on Ubuntu 18.04 Linux systems with core *i*3 processor 3.20 GHz and 16 GB RAM. Almost, the computational time varies depending on the image resolution and the number of bins existing in the histogram of the processed image. Thus, if the resolution of the image increases, then the computational time for the histogram and grey-level transformation will be raised.

From the experiments, we have observed that MIEF takes little time as it involves unidirectional fuzzy mathematical function using the hyperbolic criterion. Moreover, MIEF takes slightly more time than the proposed algorithms as MIEF is primarily concerned with restricted equivalence functions and hyperbolic membership degrees for foreground and background areas over the image pixels in ROI computation. FSE is a slow method because of the exhausted search, histogram computation and the need for computation of entropy. From the runtime analysis, the PLE computes the bi-histogram equalization, which takes considerable high execution time than MIEF. On the other hands, the RDH method takes more computation time due to its histogram computations via a reversible data hiding approach. Similarly, PLE and FSE methods require extra time because of their reiterative nature. In comparison, the proposed DIEM algorithm takes less time than MIEF, RDH, PLE, and FSE. Besides, RDH, PLE, and FSE only perform global contrast enhancement, while MIEF and DIEM carry out both local and global contrast enhancements. The average execution times of different baseline methods are shown in Fig. 8 for the all the test images with size 512×512 and it is obvious the DIEM is very fast. Therefore, the proposed algorithm more suited in real-time especially for low light drone imaging applications with regard to its accuracy and efficiency.

5. Conclusion

I n this paper, a novel intuitionistic hesitant fuzzy set based image enhancement scheme is presented for lowly illuminated dronograms where a hesitant score is used as a new way to measure image uncertainty. The proposed method initially separates a dronogram into foreground/background areas based on a global threshold and determines the membership functions by intuitionistic hesitant fuzzification approach via hyperbolic operations for membership modification. Finally, we achieve a highly informative and improved dronogram obtained by defuzzification. Results are compared with privileged methods and it is perceived that the proposed intuitionistic hesitant fuzzy set based method performs well and provides improved contrast images with better clarity and sharpness. For the lowly illuminated drone images, the proposed enhancement scheme works better because of its capability of dealing with image uncertainties by taking recourse to the intuitionistic hesitant fuzzy set. In comparison to the state-of-the-art methods, the proposed method exhibits better performance to increase both the visual quality and contrast for dronograms.

In future, the present algorithm can be improved from different directions for noisy and heavily blurred images with respect to speed up execution so that it can be applied to real-time environments. As a part of further investigation, an image enhancement model can be developed for several types of color combination drone images. The authors are currently working in these directions.

Conflict of interest

None.

Acknowledgement

This work was supported by the ESF in “Science without borders project”, reg. nr. CZ.02.2.69/0.0/0.0/16_027/0008463 within the Operational Programme Research, Development and Education.

Supplementary material

Supplementary material associated with this article can be found, in the online version, at doi:10.1016/j.ins.2019.05.069

References

[1] K. Atanassov, Intuitionistic Fuzzy Sets: Theory and Applications, Physica-Verlag, Heidelberg, New York, 1999.
[2] J. Bozek, M. Mustra, K. Delac, M. Grgic, A survey of image processing algorithms in digital mammography, Recent Advances in Multimedia Signal Processing and Communications, Springer-Verlag Berlin Heidelberg, 2009, pp. 631–657.
[3] B. Cai, X. Xu, K. Jia, C. Qing, D. Tao, Dehazenet: an end-to-end system for single image haze removal, IEEE Trans. Image Process. 25 (11) (2016) 51875198.
[4] T. Celik, Spatial entropy-based global and local image contrast enhancement, IEEE Trans. Image Process. 23 (12) (2014) 5298–5308.
[5] H.D. Cheng, H. Xu, A novel fuzzy logic approach to contrast enhancement, Pattern Recognit. 33 (2000) 799–819.
[6] H. Deng, W. Deng, X. Sun, M. Liu, C. Ye, Mammogram enhancement using intuitionistic fuzzy sets, Tran. Biomed. Eng. 64 (8) (2016) 1803–1814.
[7] P. Dvorak, B. Menze, Structured prediction with convolutional neural networks for multimodal brain tumor segmentation, in: Proceedings of the MICCAI Multimodal Brain Tumor Segmentation Challenge (BraTS), 2015, pp. 13–24.
[8] P.A. Ejegwa, An overview on intuitionistic fuzzy sets, Int. J. Sci. Technol. Res. 3 (2014) 142–145.
[9] Z. Fan, D. Bi, L. Xiong, S. Ma, L. He, W. Ding, Dim infrared image enhancement based on convolutional neural network, Neurocomputing 272 (2017) 396–404.
[10] M. Gharbi, J. Chen, J.T. Barron, S.W. Hasinoff, F. Durand, Deep bilateral learning for real-time image enhancement, ACM Trans. Gr. 36 (4) (2017) 118.
[11] K. Gu, G. Zhai, W. Lin, M. Liu, The analysis of image contrast: from quality assessment to automatic enhancement, IEEE Trans. Cybern. 46 (1) (2016) 284–297.
[12] K. Gu, G. Zhai, X. Yang, W. Zhang, Automatic contrast enhancement technology with saliency preservation, IEEE Trans. Circuits Syst. Video Technol. 25 (9) (2015) 1480–1494.
[13] K. Gu, G. Zhai, X. Yang, W. Zhang, Using free energy principle for blind image quality assessment, IEEE Trans. Multimed. 17 (1) (2015) 50–63.
[14] M. Hassaballah, A. Ghareeb, A framework for objective image quality measures based on intuitionistic fuzzy sets, Appl. Soft Comput. 57 (C) (2017) 1–24.
[15] B.K. Kim, H.S. Kang, S.O. Park, Drone classification using convolutional neural networks with merged doppler images, IEEE Geosci. Remote Sens. Lett. 14 (1) (2017) 38–42.
[16] L.P. Koh, S.A. Wich, Dawn of drone ecology: low-cost autonomous aerial vehicles for conservation, Trop. Conserv. Sci. 2 (5) (2012) 121–132.
[17] A. Laine, J. Fan, W. Yang, Wavelets for contrast enhancement of digital mammography, IEEE Eng. Med. Biol. Mag. 14 (5) (1995) 536–550.
[18] E.J. Lee, S.Y. Shin, B. Ko, C. Chang, Early sinkhole detection using a drone-based thermal camera and image processing, Infrared Phys. Technol. 78 (2016) 223–232.
[19] C. Li, Y. Yang, L. Xiao, Y. Li, Y. Zhou, J. Zhao, A novel image enhancement method using fuzzy sure entropy, Neurocomputing 215 (26) (2016) 196–211.
[20] D. Li, W. Zeng, Y. Zhao, Note on distance measure of hesitant fuzzy sets, Inf. Sci. 321 (2015) 103–115.
[21] J. Liu, C. Wu, Z. Wang, L. Wu, Reliable filter design for sensor networks using type-2 fuzzy framework, IEEE Trans. Ind. Inf. 13 (4) (2017) 1742–1752.
[22] A. Mittal, A.C. Bovik, No-reference image quality assessment in the spatial domain, IEEE Trans. Image Process. 21 (12) (2012) 4695–4708.
[23] I. Montes, N. Pal, V. Janis, S. Montes, Divergence measures for intuitionistic fuzzy sets, IEEE Trans. Fuzzy Syst. 23 (2) (2014) 444–456.
[24] N. Otsu, A threshold selection method from gray-level histograms, IEEE Trans. Syst. Man Cybern. 9 (1) (1979) 62–66.
[25] K. Panetta, Y. Zhou, S. Agaian, H. Jia, Nonlinear unsharp masking for mammogram enhancement, IEEE Trans. Inf. Technol. Biomed. 15 (2011) 918–928.
[26] G. Qian, H. Wang, X. Feng, Generalized hesitant fuzzy sets & their application in decision support system, Knowl. Based Syst. 37 (2013) 357–365.
[27] M. Ritchie, F. Fioranelli, H. Griffiths, B. Torvik, Micro-drone RCS analysis, in: Proceedings of the IEEE Radar Conference, 2015, pp. 452–456.
[28] R.M. Rodriguez, L. Martinez, V. Torra, Z.S. Xu, F. Herrera, Hesitant fuzzy sets: state of the art & future directions, Int. J. Intell. Syst. 29 (6) (2014) 495–524.
[29] F. Russo, Recent advances in fuzzy techniques for image enhancement, IEEE Trans. Instrum. Meas. 47 (6) (1998) 1428–1434.
[30] H.K. Sawant, M. Deore, A comprehensive review of image enhancement techniques, Int. J. Comput. Technol. Electr. Eng. 19 (2) (2010) 39–44.
[31] L. Shen, Z. Yue, F. Feng, Q. Chen, S. Liu, J. Ma, MSR-net: low-light image enhancement using deep convolutional network, 2017, CoRR, arXiv: 1711.02488.
[32] N. Tajbakhsh, J.Y. Shin, S.R. Gurudu, R.T. Hurst, C.B. Kendall, M.B. Gotway, J. Liang, Convolutional neural networks for medical image analysis: full training or fine tuning? IEEE Tran. Med. Imaging 35 (5) (2016) 1299–1312.
[33] H.R. Tizhoosh, Fuzzy Technique in Image Processing, Spring-Verlag, Berlin Heidelberg, 2000, pp. 137–146.
[34] Y. Wang, J. Zhang, Y. Cao, Z. Wang, A deep CNN method for underwater image enhancement, in: Proceedings of the IEEE International Conference on Image Processing (ICIP), 2017, p. 2017.
[35] Z. Wang, A.C. Bovik, H.R. Sheikh, E.P. Simoncelli, Image quality assessment: from error visibility to structural similarity, IEEE Trans. Image Process. 13 (4) (2004) 600–612.
[36] Z. Wang, A.C. Bovik, A universal image quality index, IEEE Signal Process. Lett. 9 (3) (2002) 81–84.
[37] H.T. Wu, S. Tang, J. Huang, Y.Q. Shi, A novel reversible data hiding method with image contrast enhancement, Signal. Process. Image Commun. 62 (2018) 64–73.
[38] B. Xiao, H. Tang, Brightness and contrast controllable image enhancement based on histogram specification, Neurocomputing 275 (C) (2017) 1–12.
[39] K. Xiaodong, S. Xiubao, L. Yuan, C. Qian, G. Guohua, Single infrared image enhancement using a deep convolutional neural network, Neurocomputing 332 (2018) 119–128.
[40] Z.S. Xu, Hesitant Fuzzy Sets Theory, Studies in Fuzziness & Soft Computing, Springer International Publishing, 2014.
[41] L.A. Zadeh, Fuzzy sets, Inf. Comput. 8 (1965) 338–353.
[42] Y. Zhao, J. Wang, F. Yan, Y. Shen, Adaptive sliding mode fault-tolerant control for type-2 fuzzy systems with distributed delays, Inf. Sci. 473 (2019) 227–238.
[43] D. Zikic, Y. Ioannou, A. Criminisi, M. Brown, Segmentation of brain tumor tissues with convolutional neural networks, in: Proceedings of the MICCAI Multimodal Brain Tumor Segmentation Challenge (BraTS), 2014, p. 3639.
[44] https://github.com/OpenDroneMap/odm-data.